

Copyright  
by  
Stewart Victor McDougall  
2022

The Report Committee for Stewart Victor McDougall  
certifies that this is the approved version of the following report:

## **Early Response of Ablative Materials to Arcjet Testing**

APPROVED BY

SUPERVISING COMMITTEE:

---

Fabrizio Bisetti, Supervisor

---

Noel Clemens

# Early Response of Ablative Materials to Arcjet Testing

by

Stewart Victor McDougall

## REPORT

Presented to the Faculty of the Graduate School of

The University of Texas at Austin

in Partial Fulfillment

of the Requirements

for the Degree of

**MASTER OF SCIENCE IN ENGINEERING**

THE UNIVERSITY OF TEXAS AT AUSTIN

May 2022

## Acknowledgments

Special thanks to my advisor, Dr. Fabrizio Bisetti, for the many hours spent imparting knowledge, reinforcing learning, and patiently reviewing my work. It has been a privilege to learn from him on a regular basis. Many thanks also to Dr. Noel Clemens for reviewing this paper and giving his feedback, as well as ensuring that my degree progress was on track. My thanks as well to Aditya Vinod, who gave me excellent critiques and guidance throughout the project and helped immeasurably with formatting. Finally, I would like to thank my family for their love and support over the last year and a half, and for making an honest effort to appear interested every time we talked.

# Early Response of Ablative Materials to Arcjet Testing

Stewart Victor McDougall, M.S.E.  
The University of Texas at Austin, 2022

Supervisor: Fabrizio Bisetti

The initial temperature response of phenolic injected carbon ablators (PICA) under arcjet test conditions is modeled by implementing heat conduction, radiation, and pyrolysis using publicly available material properties. Prior to significant pyrolyzation occurring, good agreement is found between experimental results and model results. Key processes during the initial temperature response are found to be heat conduction and radiation. The modeling approach proposed in this work is novel and can be combined easily with a statistical framework that implements Bayesian inference of material thermal properties and stagnation heat flux from multiple thermocouple data. Refined model results are intended for use in inference of material properties through comparison to experimental data.

# Table of Contents

<b>Acknowledgments</b>	<b>4</b>
<b>Abstract</b>	<b>5</b>
<b>List of Tables</b>	<b>7</b>
<b>List of Figures</b>	<b>8</b>
<b>Chapter 1. Introduction</b>	<b>9</b>
<b>Chapter 2. Methodology</b>	<b>11</b>
2.1 Assumptions . . . . .	11
2.2 Energy model . . . . .	12
2.3 Boundary conditions . . . . .	14
2.4 Material model . . . . .	15
2.5 Reference test case and implementation . . . . .	20
<b>Chapter 3. Results and Discussion</b>	<b>26</b>
3.1 Sensitivity to pyrolysis model . . . . .	26
3.2 Material property effects . . . . .	36
<b>Chapter 4. Conclusion</b>	<b>42</b>

# List of Tables

- 2.1 Competitive pyrolysis model parameters. . . . . 18
- 2.2 FIAT1D/CMA pyrolysis model parameters. . . . . 20
- 2.3 Model PICA material properties. . . . . 22
- 2.4 Thermocouple (TC) placement options from Milos and Chen [1]. . . . . 24
  
- 3.1 Virgin and char material properties. . . . . 38

## List of Figures

2.1	Cross-section of a pyrolyzing material in an external flow showing different regions and processes. . . . .	16
2.2	Progression of the competitive reaction. [2] . . . . .	16
2.3	Axisymmetric iso-q geometry scaled by sample radius, $R$ ; the vertical axis corresponds to the axis of rotation. . . . .	21
2.4	Heat flux scaled by the stagnation point heat flux to the surface as a function of streamlength, the distance along the surface from the stagnation point[3]. . . . .	22
2.5	TC locations scaled by sample radius, $R$ . . . . .	23
3.1	Axial TCs for models of increasing complexity along with experimental data, $\alpha = 2.0$ . . . . .	27
3.2	Radial TCs for models of increasing complexity along with experimental data, $\alpha = 2.0$ . . . . .	28
3.3	Axial TCs temperature response for different pyrolysis models. . . . .	29
3.4	Radial TCs temperature response for different pyrolysis models. . . . .	30
3.5	Specific enthalpy for TACOT. . . . .	31
3.6	TACOT specific enthalpy of pyrolysis, $h_g - \bar{h}$ . . . . .	32
3.7	Rate of change of density for different material models, $-\partial\tilde{\rho}_s/\partial t$ . . . . .	33
3.8	Solid density fraction remaining in the material, FIAT1D/CMA model, $\alpha = 2.0$ . . . . .	34
3.9	Temperature response close to the surface, FIAT1D/CMA model, $\alpha = 2.0$ . . . . .	35
3.10	Axial TCs temperature response with conduction, pyrolysis, and radiation. . . . .	36
3.11	Radial TCs temperature response with conduction, pyrolysis, and radiation. . . . .	37
3.12	Axial TCs for differing material properties (dimensionless response). . . . .	38
3.13	Radial TCs for differing material properties (dimensionless response). . . . .	39
3.14	Axial TCs for differing material properties (dimensional response). . . . .	39
3.15	Radial TCs for differing material properties (dimensional response). . . . .	40

# Chapter 1

## Introduction

The material response of surfaces exposed to hypersonic flows remains a complex process and its modeling is the subject of ongoing research. High speed flows such as those experienced during orbital re-entry or hypersonic flight subjects vehicles to heat loads in excess of  $4.8 \text{ MW/m}^2$ , necessitating heat shielding for the payload; heat shield surface temperatures can approach  $3000 \text{ K}$ [4]. However, this increases vehicle mass, resulting in higher fuel costs and reducing payload. One way to reduce weight is to use ablative materials, which undergo endothermic chemical decomposition and emit gaseous byproducts that mix with boundary layer gases.

Due to the difficulty of replicating these extreme conditions in experimental settings, many efforts have been made to develop computational models. Challenges in producing a computational model include the presence of thermal or chemical nonequilibrium [5], coupling of external flow to the material at the exposed surface, and surface recession. One of the most fundamental challenges is the accurate measurement of the material properties of the ablative material itself. Phenolic Impreganted Carbon Ablator (PICA), for instance, was first used by NASA in the Stardust comet sample return mission and the Mars 2001 mission [6] for thermal protection. It was later used successfully in the Mars Science Laboratory mission [7]. This material is made of a highly porous carbon fiberform structure which does not pyrolyze but may oxidize or sublime when exposed to hot gases and a phenolic resin which is added to the fiberform. The phenolic resin breaks down at high temperatures, releasing gaseous products and leaving behind char, which is mostly carbon [8]. Each of these solid phases have densities,

thermal conductivities, and specific heats that vary as temperature increases and pyrolysis occurs. Many experimental studies have been conducted to measure properties and relate them to the extent of pyrolysis [9–11]. Thermal conductivity in the solid is often orthotropic due to PICA being manufactured in layers [3, 12]. The composition of PICA may vary based on the type of fibrous preform used and the amount and type of phenolic resin it is infused with. However, the most updated PICA v.3.3 model used by NASA is ITAR protected [13], as may be the case with models for future ablative materials. Furthermore, material properties change slightly depending on its manufacturing process and composition. This study models the physical processes related to heat transfer in a PICA-like material. Working with a dimensionless formulation, the ability to scale initial temperature response based on density, specific heat, and orthotropy of thermal conductivity is demonstrated. A model of this type is characterized by a few physical parameters and is well suited to the inference of those material properties for other thermal protective system (TPS) materials based on experimental results. Significant to this study are separation of the effects of individual physical processes on the overall material response. By focusing on times and environments which minimize the effects of pyrolyzation, ablative recession at the surface, and convective effects of pyrolysis gas, inference of thermal characteristics is possible in relative isolation. This is especially helpful since rigorous modeling of these phenomena can require non-equilibrium reaction calculations, flow field coupling, and surface recession, which are computationally expensive and may be less well-understood.

# Chapter 2

## Methodology

This study sought to accurately model heat transfer in an ablative material for the purpose of inference of material properties, specifically thermal conductivity and heat capacity. It was not intended as a computational model for the complete pyrolysis and ablation processes when many such approaches already exist, but to model a regime where very little pyrolysis is occurring in the material. For that reason, although this study makes comparisons with the full range of experimental data available, the focus is on accurate modeling of the first few seconds of arcjet experiments when temperature histories from thermocouple measurements are most sensitive to heat transfer only.

### 2.1 Assumptions

The set of physical processes we sought to implement are heat conduction, radiation at the exposed surface, and energy exchange through the chemical reactions of pyrolysis. Convection of pyrolysis gases, boundary layer interactions, and surface recession were not included, with a lower heating condition and short time scales chosen to minimize these effects. Crucially, the initial temperature for simulations was set to a uniform 300 K, although a nonuniform temperature distribution was observed in the experimental data. Finally, specific heat and thermal conductivity values were assumed to be uniform across the sample and constant over the same initial period. Governing equations for these processes were specified as discussed below in the energy model, the material model, and the boundary conditions used.

## 2.2 Energy model

The thermal model is based on the equation for unsteady heat conduction with a source term:

$$\rho_s C_p \frac{\partial T}{\partial t} = \nabla \cdot (\kappa \cdot \nabla T) + (h_g - \bar{h}) \frac{\partial \rho_s}{\partial t}. \quad (2.1)$$

The terms here are the unsteady term, heat conduction, and a source term due to pyrolysis. In this equation,  $\rho_s$  is density and  $C_p$  is the specific heat. The gaseous specific enthalpy,  $h_g$ , is a function of pressure and temperature. This is similar to the FIAT1D model[6]; however, FIAT includes a convection rate for pyrolysis gases, while in the current model convection of pyrolysis gas is not included. The quantity  $\bar{h}$  is termed the partial heat of charring by Milos and Chen [6] and is discussed in detail below. In equation (2.1),  $\kappa$  is a tensor describing the thermal conductivity for an orthotropic material. We define  $\alpha$  as the ratio between thermal conductivity in the radial or “in plane” direction,  $\kappa_{\parallel}$ , and the axial or “through the thickness” direction,  $\kappa_{\perp}$ . The thermal conductivity tensor is:

$$\kappa = \begin{bmatrix} \kappa_{\parallel} & 0 \\ 0 & \kappa_{\perp} \end{bmatrix} = \kappa_{\perp} \begin{bmatrix} \alpha & 0 \\ 0 & 1 \end{bmatrix}. \quad (2.2)$$

For an explanation of  $\bar{h}$ , consider the definition of the mass fractions of virgin material, char material, and pyrolysis gas in a sample:

$$Y_v = \rho_{v,s} / \rho_{\text{tot}}, \quad (2.3)$$

$$Y_c = \rho_{c,s} / \rho_{\text{tot}}, \quad (2.4)$$

$$Y_g = \rho_g / \rho_{\text{tot}}. \quad (2.5)$$

Here,  $\rho_{v,s}$  is the density of virgin material in the solid at a given time,  $\rho_{c,s}$  is the density of char in the solid at a given time,  $\rho_g$  is the density of the pyrolysis gas, and  $\rho_{\text{tot}}$  is the total density of the solid and gas phases and remains constant. The rate of change of the specific enthalpy during pyrolysis reads:

$$\dot{h}_{\text{pyro}} = h_v \frac{\partial Y_v}{\partial t} + h_c \frac{\partial Y_c}{\partial t} + h_g \frac{\partial Y_g}{\partial t}. \quad (2.6)$$

The extent of the reaction is  $1 - Y_v$ , and the mass fractions of the char and gaseous phases are related to the final mass fractions of the char and gaseous phases as

$$Y_c = (1 - Y_v)Y_{cf}, \quad (2.7)$$

$$Y_g = (1 - Y_v)Y_{gf}. \quad (2.8)$$

Since at the end of the reaction only the char and gas phases exist,

$$Y_{cf} + Y_{gf} = 1. \quad (2.9)$$

The rates of change of the char and gas phases are

$$\frac{\partial Y_c}{\partial t} = -Y_{cf} \frac{\partial Y_v}{\partial t}, \quad (2.10)$$

$$\frac{\partial Y_g}{\partial t} = -(1 - Y_{cf}) \frac{\partial Y_v}{\partial t}. \quad (2.11)$$

Substituting into Eq. 2.6 gives

$$\begin{aligned} \dot{h}_{\text{pyro}} &= \frac{\partial Y_v}{\partial t} [h_v - h_c Y_{cf} - h_g (1 - Y_{cf})] \\ &= (1 - Y_{cf}) \frac{\partial Y_v}{\partial t} \left( \frac{h_v - Y_{cf} h_c}{1 - Y_{cf}} - h_g \right). \end{aligned} \quad (2.12)$$

From Eq. 2.11, it follows that for the first two terms

$$(1 - Y_{cf}) \frac{\partial Y_v}{\partial t} = -\frac{\partial Y_g}{\partial t} = \frac{\partial Y_s}{\partial t}. \quad (2.13)$$

Furthermore, the final char mass fraction is s

$$Y_{cf} = \frac{\rho_{c,f}}{\rho_{\text{tot}}} = \frac{\rho_c}{\rho_v}, \quad (2.14)$$

where  $\rho_v$  is the initial density of virgin PICA and  $\rho_c$  is the final (char) density in PICA; both of these are treated as constants. Substituting the above into Eq. 2.12 gives

$$\dot{h}_{\text{pyro}} = \frac{1}{\rho_v} \frac{\partial \rho_s}{\partial t} \left( \frac{\rho_v h_v - \rho_c h_c}{\rho_v - \rho_c} - h_g \right) = \frac{1}{\rho_v} \frac{\partial \rho_s}{\partial t} (\bar{h} - h_g). \quad (2.15)$$

## 2.3 Boundary conditions

The energy balance at the exposed surface, neglecting the contributions of pyrolysis gas and char, is taken to be

$$\kappa \nabla T \cdot \underline{\mathbf{n}} + \sigma \epsilon T_w^4 = q, \quad (2.16)$$

where  $T_w$  is the surface temperature and  $\sigma$  is the Stefan-Boltzmann constant. Emissivity  $\epsilon$  is a weak function of temperature in char and is taken to be 0.89 for a fully charred surface [10, 14]. The cold wall heat flux  $q$  is prescribed along the sample's surface as described in section 2.5. Eq. 2.16 serves as a boundary condition at the exposed material surface. The temperature at the bottom surface of the material is assumed constant, resulting in a Dirichlet boundary condition at this surface (Eq. 2.17). A homogeneous Neumann condition is applied on the axis (Eq. 2.18).

$$T = T_0 \quad (2.17)$$

$$\left. \frac{\partial T}{\partial r} \right|_{r=0} = 0 \quad (2.18)$$

A method to nondimensionalize both temperature and time by scaling factors was employed as follows. Reference temperature and reference time are defined as follows:

$$T_{\text{ref}} = \frac{q_0 R}{\kappa_{\perp}}, \quad (2.19)$$

$$t_{\text{ref}} = \frac{\rho_v C_{p,0} R^2}{\kappa_{\perp}}, \quad (2.20)$$

where  $\rho_v$  is a constant equal to the density of the virgin material,  $q_0$  is the heat flux into the material at the stagnation point,  $R$  is the sample radius, and  $C_{p,0}$  is the initial specific heat of the solid. Using this method, dimensionless spatial coordinates, temperature, time, thermal conductivity, and heat flux are defined as follows:

$$[\tilde{r}, \tilde{z}] = \frac{[r, z]}{R}, \quad (2.21)$$

$$\tilde{T} = \frac{T - T_0}{T_{\text{ref}}}, \quad (2.22)$$

$$\tilde{t} = \frac{t}{t_{\text{ref}}}, \quad (2.23)$$

$$\tilde{\kappa} = \frac{\kappa}{\kappa_{\perp}} = \begin{bmatrix} \alpha & 0 \\ 0 & 1 \end{bmatrix}, \quad (2.24)$$

$$\tilde{q} = \frac{q}{q_0}, \quad (2.25)$$

$$\tilde{\rho}_s = \frac{\rho_s}{\rho_v}, \quad (2.26)$$

$$\tilde{h} = \frac{h}{h_{\text{ref}}} = \frac{h}{C_{p,0}T_{\text{ref}}}. \quad (2.27)$$

In nondimensional form, then, the energy balance equation is expressed as:

$$\frac{\partial \tilde{T}}{\partial \tilde{t}} = \tilde{\nabla} \cdot (\tilde{\kappa} \cdot \tilde{\nabla} \tilde{T}) + (\tilde{h}_g - \tilde{h}) \frac{\partial \tilde{\rho}_s}{\partial \tilde{t}}. \quad (2.28)$$

To determine the rate of change of the density of the solid, two different methods of modeling the pyrolysis reactions were employed.

## 2.4 Material model

In a pyrolyzing TPS material, heat conducted from the surface causes the ablative material to decompose, releasing gases that flow to the surface. The residual solid is carbon char and carbon fibers. As a whole, the ablative material can be thought of as a combination of virgin material, pyrolysis gas, carbon fibers, and char. A schematic of a pyrolyzing material is shown below in Fig. 2.1

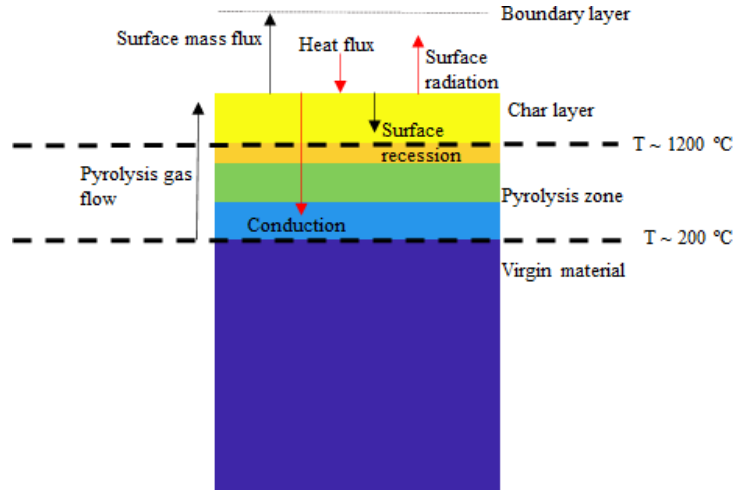


Figure 2.1: Cross-section of a pyrolyzing material in an external flow showing different regions and processes.

This creates a coupled system with the material model connected to the energy equation through the source term. To simulate PICA's material response to external heating, two different models were used: the first was based on the model proposed by Torres-Herrador, et. al. [2] using the concept of competitive chemical reactions, and the second was modeled after Aerotherm's Charring Material Thermal Response and Ablation Program (CMA) [15] and early versions of Fully Implicit Ablation Thermal Response (FIAT) code [6]. The competitive model used was developed by Torres-Herrador, et. al. [2] and allows the material to decompose by different reactions in a branching manner as shown in Fig. 2.2.

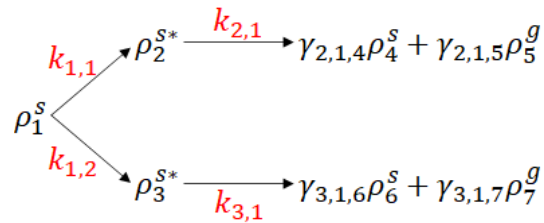


Figure 2.2: Progression of the competitive reaction. [2]

This means that the initial solid material decomposes into multiple intermediate species which can further decompose into the final products. For each component in the reaction, there is an associated rate of production as the intermediate and final species are created through earlier reactions as well as a rate of destruction of the component as it decomposes through the different competitive branches towards the products. The overall rate of change of the density of component  $i$ , then, is given by

$$\frac{\partial \rho_i}{\partial t} = - \sum_{j=1}^{n_i^P} k_{i,j} \rho_i + \sum_{j=1}^n \sum_{l=1}^{n_j^P} k_{j,l} \gamma_{j,l,i} \rho_j, \quad (2.29)$$

where  $n_i^P$  is the number of competitive reactions by which component  $i$  decays into subspecies  $j$  and  $\gamma_{j,l,i}$  is the mass ratio of species  $j$  in the products. By conservation of mass,  $\gamma_{j,l,i} = (1 - \gamma_{j,l,i-1})$ . In this model, as shown in Figure 2.2, the initial solid,  $\rho_1^s$ , decomposes into intermediate solids,  $\rho_2^s$  and  $\rho_3^s$ , which further decompose into solid species,  $\rho_4^s$  and  $\rho_6^s$ , along with gaseous species,  $\rho_5^g$  and  $\rho_7^g$ , respectively.

The kinetic rate of the decomposition of  $i$  into  $j$  through reaction  $P_{i,j}$  is modeled with a first order Arrhenius equation of the form

$$k_i = \mathcal{A}_i \exp(-\varepsilon_i/\mathcal{R}T), \quad (2.30)$$

where  $\mathcal{A}_i$  is the pre-exponential factor,  $\mathcal{R}$  is the universal gas constant, and  $\varepsilon_i$  is the activation energy for the reaction. Density in the solid material is then

$$\rho_s = \sum_{i=1}^{n_s} \epsilon_i \rho_i, \quad (2.31)$$

where  $\epsilon_i$  is the volume fraction of component  $i$ . The ODE solved for the rate of change of component densities can then be written in matrix form as follows:

$$\frac{d}{dt} \begin{pmatrix} \rho_1^s \\ \rho_2^{s*} \\ \rho_3^{s*} \\ \rho_4^s \\ \rho_5^g \\ \rho_6^s \\ \rho_7^g \end{pmatrix} = \begin{bmatrix} -(k_{1,1} + k_{1,2}) & 0 & 0 & 0 & 0 & 0 & 0 \\ k_{1,1} & -k_{2,1} & 0 & 0 & 0 & 0 & 0 \\ k_{1,2} & 0 & -k_{3,1} & 0 & 0 & 0 & 0 \\ 0 & \gamma_{2,1,4} k_{2,1} & 0 & 0 & 0 & 0 & 0 \\ 0 & \gamma_{2,1,5} k_{2,1} & 0 & 0 & 0 & 0 & 0 \\ 0 & 0 & \gamma_{3,1,6} k_{3,1} & 0 & 0 & 0 & 0 \\ 0 & 0 & \gamma_{3,1,7} k_{3,1} & 0 & 0 & 0 & 0 \end{bmatrix} \begin{pmatrix} \rho_1^s \\ \rho_2^{s*} \\ \rho_3^{s*} \\ \rho_4^s \\ \rho_5^g \\ \rho_6^s \\ \rho_7^g \end{pmatrix}. \quad (2.32)$$

The values for the rate coefficients, activation energies, and mass coefficients for the competitive model are shown below in Table 2.1.

Table 2.1: Competitive pyrolysis model parameters.

Parameter	Value	Parameter	Value
$\log_{10}(\mathcal{A}_{1,1})$	2.019	$\varepsilon_{1,1}$	32618.482
$\log_{10}(\mathcal{A}_{1,2})$	14.292	$\varepsilon_{1,2}$	143273.910
$\log_{10}(\mathcal{A}_{2,1})$	0.442	$\varepsilon_{2,1}$	51783.980
$\log_{10}(\mathcal{A}_{3,1})$	0.993	$\varepsilon_{3,1}$	31087.851
$\gamma_{2,1,5}$	0.163	$\gamma_{3,1,7}$	0.244

The reaction rate coefficients are nondimensionalized using the reference quantities as follows:

$$\tilde{k}_i = (A_i t_{\text{ref}}) \exp\left(-\frac{\varepsilon_i/R}{\tilde{T}(T_{\text{ref}}) + T_0}\right). \quad (2.33)$$

In nondimensional matrix form, the system of equations to be solved is then

$$-\tilde{\nabla} \cdot \underline{\underline{c}} \otimes \tilde{\nabla} \begin{bmatrix} \tilde{T} \\ \tilde{\rho}_1^s \\ \tilde{\rho}_2^{s*} \\ \tilde{\rho}_3^{s*} \\ \tilde{\rho}_4^s \\ \tilde{\rho}_5^g \\ \tilde{\rho}_6^s \\ \tilde{\rho}_7^g \end{bmatrix} - \begin{bmatrix} 0 & 0 & 0 & 0 & 0 & 0 & 0 & 0 \\ 0 & -(\tilde{k}_{1,1} + \tilde{k}_{1,2}) & 0 & 0 & 0 & 0 & 0 & 0 \\ 0 & \tilde{k}_{1,1} & -\tilde{k}_{2,1} & 0 & 0 & 0 & 0 & 0 \\ 0 & \tilde{k}_{1,2} & 0 & -\tilde{k}_{3,1} & 0 & 0 & 0 & 0 \\ 0 & 0 & \gamma_{2,1,4} \tilde{k}_{2,1} & 0 & 0 & 0 & 0 & 0 \\ 0 & 0 & \gamma_{2,1,5} \tilde{k}_{2,1} & 0 & 0 & 0 & 0 & 0 \\ 0 & 0 & 0 & \gamma_{3,1,6} \tilde{k}_{3,1} & 0 & 0 & 0 & 0 \\ 0 & 0 & 0 & \gamma_{3,1,7} \tilde{k}_{3,1} & 0 & 0 & 0 & 0 \end{bmatrix} \begin{bmatrix} \tilde{T} \\ \tilde{\rho}_1^s \\ \tilde{\rho}_2^{s*} \\ \tilde{\rho}_3^{s*} \\ \tilde{\rho}_4^s \\ \tilde{\rho}_5^g \\ \tilde{\rho}_6^s \\ \tilde{\rho}_7^g \end{bmatrix} = \begin{bmatrix} 0 \\ 0 \\ 0 \\ 0 \\ 0 \\ 0 \\ 0 \\ 0 \end{bmatrix} \quad (2.34)$$

$$\underline{\mathbf{c}} = \begin{bmatrix} 1 & 0 & 0 & \cdots & 0 \\ 0 & \alpha & 0 & \cdots & 0 \\ 0 & 0 & 0 & \cdots & 0 \\ \vdots & \vdots & \vdots & \ddots & \vdots \\ 0 & 0 & 0 & \cdots & 0 \end{bmatrix}. \quad (2.35)$$

A second model was taken from FIAT1D/CMA[6, 15]. This model has two components which are consumed separately and a reinforcing material component (fiberform in PICA's case) which is not consumed. Density in the solid is given by

$$\rho_s = \Gamma(\rho_A + \rho_B) + (1 - \Gamma)\rho_C, \quad (2.36)$$

where  $\rho_A$  is the density of the first resin component in PICA,  $\rho_B$  is the density of the second resin component, and  $\rho_C$  is the density of the fiberform. The volume fraction of the resin is  $\Gamma$  and  $(1 - \Gamma)$  is the volume fraction of the reinforcing material. As in version 1 of FIAT, porosity does not change over time [6]. Each of the components decomposes as

$$\frac{\partial \rho_i}{\partial t} = -B_i \exp(-E_i/T) \rho_{v,i} \left( \frac{\rho_i - \rho_{c,i}}{\rho_{v,i}} \right)^{\Psi_i}, \quad (2.37)$$

where  $B_i$  is the rate coefficient for that component,  $E_i$  is the activation temperature of the reaction and  $\Psi_i$  is the order of the reaction.  $\rho_{v,i}$  and  $\rho_{c,i}$  are the initial and residual densities of the component, respectively. From the CMA inputs used in Tran, et. al.[10] and Rindal, et. al. [11] the A and B decomposing components have  $\Psi_i=3$ , while component C does not decompose. CMA values for pre-exponential factors and activation temperature are shown in Table 2.2. The rate of change of density of the solid in dimensionless form reads,

$$\frac{\partial \tilde{\rho}_s}{\partial \tilde{t}} = \frac{\partial \rho_s}{\partial t} \left( \frac{t_{\text{ref}}}{\rho_v} \right). \quad (2.38)$$

Table 2.2: FIAT1D/CMA pyrolysis model parameters.

solid component	$B_i, \text{s}^{-1}$	$E_i, \text{K}$	$\Psi_i$	$\rho_v, \text{kg/m}^3$	$\rho_c, \text{kg/m}^3$
<i>A</i>	4.48e9	20444	3.0	973	519
<i>B</i>	1.40e4	8556	3.0	324	0
<i>C</i>	N/A	N/A	N/A	1560	1560

## 2.5 Reference test case and implementation

The experimental data used for comparison were taken from the series of experiments by F.S. Milos and Y.K. Chen at the NASA Ames Aerodynamic Heating Facility [1, 3]. The study measured the response of PICA for various values of stagnation point cold wall heat flux,  $q_0$ . Since the focus of this comparison is on verification of material properties in the absence of pyrolysis, a test case with a relatively low cold-wall heat flux  $q_0 = 169 \text{ W/cm}^2$  and multiple thermocouple data sets was chosen. This study used a sample geometry known as “iso-q,” which retains the same surface profile as it ablates. The specific geometry normalized by the sample radius for our axisymmetric case is shown in Fig. 2.3. The shoulder radius is 12.5% of the sample radius.

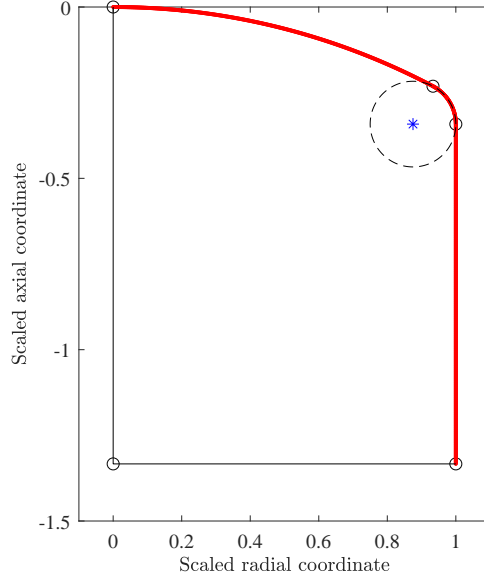


Figure 2.3: Axisymmetric iso-q geometry scaled by sample radius,  $R$ ; the vertical axis corresponds to the axis of rotation.

This setup has non-negligible sidewall heating as predicted by CFD simulations, resulting in orthotropic thermal conduction effects[16]. The spatial distribution of the heat flux from a CFD calculation by Milos and Chen is shown in Fig. 2.4[3]. This was generated using the Data-Parallel Line Relaxation (DPLR) Navier-Stokes solver for a nonequilibrium flow to calculate the arcjet flow field and validated by comparing calculated and measured stagnation point enthalpies.

This study used an equivalent scaling factor for the heat flux applied to the model along its surface to prescribe the heat flux boundary condition in Eq. 2.16. Because this study focuses on minimizing the effect of physical processes other than heat transfer, shorter simulation times were used and surface recession was neglected. With a constant geometry, the heat flux remained constant in time as well.

The material quantities used to nondimensionalize the governing equations were gathered from previously published studies by H.K. Tran, et. al. [9, 10], M.A. Covington,

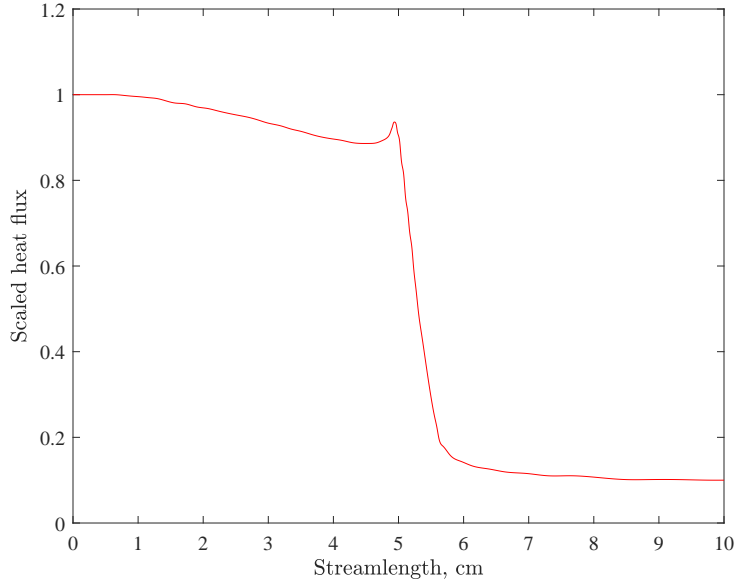


Figure 2.4: Heat flux scaled by the stagnation point heat flux to the surface as a function of streamlength, the distance along the surface from the stagnation point[3].

et. al. [14], Rindal, et. al. [11], and the TPSx material database [17]. Values for these quantities are shown in table 2.3, except where specified otherwise.

Table 2.3: Model PICA material properties.

$\rho_v, \text{kg/m}^3$	$\rho_c, \text{kg/m}^3$	$C_{p,0}, \text{kJ/kg-K}$	$\kappa_{\perp}, \text{W/m-K}$
280	221	1.40	0.358

This is a marked simplification, since it is known that density, specific heat, and thermal conductivity all change as the material pyrolyzes. Some of the relative effects of scaling these quantities by a constant are presented in chapter 3. However, change in these properties in an unsteady fashion over time and in a spatially nonuniform fashion within the material is not modeled here, with focus being on the initial material response when temperatures are lower and pyrolysis is minimal.

MATLAB’s PDE solver was selected to model conduction in the material. This

toolbox includes functions to generate a mesh of triangular elements for a given geometry, and solves partial differential equations with a finite element method. Meshes of various sizes were tested, and it was found that the fidelity of the material temperature response with pure conduction was related to the magnitude of the heat flux applied. For our chosen heating case of  $169 \text{ W/cm}^2$  at the stagnation point, a mesh size of 6,585 elements was selected. The smallest element has side of length 0.5 mm. Probes were placed at the same locations as those in the experimental model. These corresponding thermocouple locations are plotted with the mesh used in Fig. 2.5 and recorded in table 2.4.

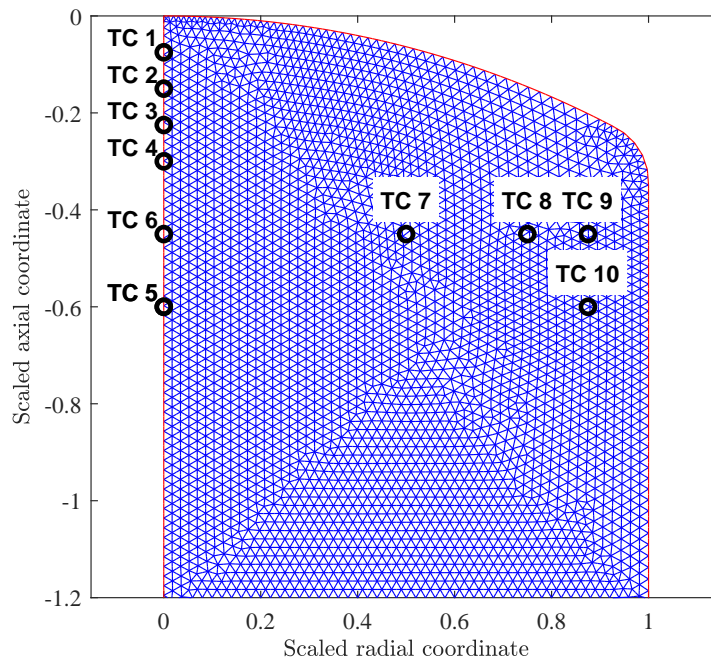


Figure 2.5: TC locations scaled by sample radius,  $R$ .

A second order operator splitting method was used to improve computational efficiency. For each time step, a PDE was first solved for half a time step accounting solely for heat conduction, with the appropriate boundary conditions applied as previously

Table 2.4: Thermocouple (TC) placement options from Milos and Chen [1].

TC number	TC placement option	axial depth, cm	radial distance, cm
1	A	0.381	0.000
2	A	0.762	0.000
3	A	1.143	0.000
4	A	1.524	0.000
5	A and D	3.048	0.000
6	D	2.286	0.000
7	D	2.286	2.540
8	D	2.286	3.810
9	D	2.286	4.445
10	D	3.048	4.445

described.

$$\frac{\partial \tilde{T}}{\partial \tilde{t}} = \tilde{\nabla} \cdot (\tilde{\kappa} \cdot \tilde{\nabla} \tilde{T}) \quad (2.39)$$

Solving the PDE over half of a time step yields an intermediate temperature field,  $\tilde{T}^* = \tilde{T}^*(\tilde{r}, \tilde{y}; \tilde{t}_{n+\frac{1}{2}})$ . This is then taken to be the initial conditions to solve a system of ODEs for the seven phases and temperature at each element over a full time step from  $\tilde{t}_n$  to  $\tilde{t}_{n+1}$  according to equations 2.29 and 2.31. The heat of pyrolysis is also taken into account,

so that the system of equations the ODE solver handles is

$$\begin{aligned}
& \begin{bmatrix} 1 & -(\tilde{h}_g - \tilde{h}) & -(\tilde{h}_g - \tilde{h}) & -(\tilde{h}_g - \tilde{h}) & -(\tilde{h}_g - \tilde{h}) & 0 & -(\tilde{h}_g - \tilde{h}) & 0 \\ 0 & 1 & 0 & 0 & 0 & 0 & 0 & 0 \\ 0 & 0 & 1 & 0 & 0 & 0 & 0 & 0 \\ 0 & 0 & 0 & 1 & 0 & 0 & 0 & 0 \\ 0 & 0 & 0 & 0 & 1 & 0 & 0 & 0 \\ 0 & 0 & 0 & 0 & 0 & 1 & 0 & 0 \\ 0 & 0 & 0 & 0 & 0 & 0 & 1 & 0 \\ 0 & 0 & 0 & 0 & 0 & 0 & 0 & 1 \end{bmatrix} \frac{\partial}{\partial \tilde{t}} \begin{bmatrix} \tilde{T} \\ \tilde{\rho}_1^s \\ \tilde{\rho}_2^{s*} \\ \tilde{\rho}_3^{s*} \\ \tilde{\rho}_4^s \\ \tilde{\rho}_5^g \\ \tilde{\rho}_6^s \\ \tilde{\rho}_7^g \end{bmatrix} \\
& - \begin{bmatrix} 0 & 0 & 0 & 0 & 0 & 0 & 0 & 0 \\ 0 & -(\tilde{k}_{1,1} + \tilde{k}_{1,2}) & 0 & 0 & 0 & 0 & 0 & 0 \\ 0 & \tilde{k}_{1,1} & -\tilde{k}_{2,1} & 0 & 0 & 0 & 0 & 0 \\ 0 & \tilde{k}_{1,2} & 0 & -\tilde{k}_{3,1} & 0 & 0 & 0 & 0 \\ 0 & 0 & \gamma_{2,1,4}\tilde{k}_{2,1} & 0 & 0 & 0 & 0 & 0 \\ 0 & 0 & \gamma_{2,1,5}\tilde{k}_{2,1} & 0 & 0 & 0 & 0 & 0 \\ 0 & 0 & 0 & \gamma_{3,1,6}\tilde{k}_{3,1} & 0 & 0 & 0 & 0 \\ 0 & 0 & 0 & \gamma_{3,1,7}\tilde{k}_{3,1} & 0 & 0 & 0 & 0 \end{bmatrix} \begin{bmatrix} \tilde{T} \\ \tilde{\rho}_1^s \\ \tilde{\rho}_2^{s*} \\ \tilde{\rho}_3^{s*} \\ \tilde{\rho}_4^s \\ \tilde{\rho}_5^g \\ \tilde{\rho}_6^s \\ \tilde{\rho}_7^g \end{bmatrix} = \begin{bmatrix} 0 \\ 0 \\ 0 \\ 0 \\ 0 \\ 0 \\ 0 \\ 0 \end{bmatrix}. \quad (2.40)
\end{aligned}$$

The temperature field obtained in this manner is then advanced over a half time step accounting for conduction and boundary conditions using Eq. 2.39.

## Chapter 3

### Results and Discussion

#### 3.1 Sensitivity to pyrolysis model

In order to analyze the significance of specific physical processes, individual terms of the energy equation were implemented sequentially and compared to the experiments conducted by F.S. Milos and Y.-K. Chen at NASA Ames [1]. PICA sample geometry and thermocouple locations were identical to those shown in Fig. 2.5. Using the thermal model in Eq. 2.1, terms can be turned off or turned on to demonstrate the relative importance of those processes as modeled in the thermal response of the sample. Simulation results for various conditions are shown together with experimental results in Figs. 3.1 and 3.2. Experimental results are shown with a  $\pm 5\%$  uncertainty band [1].

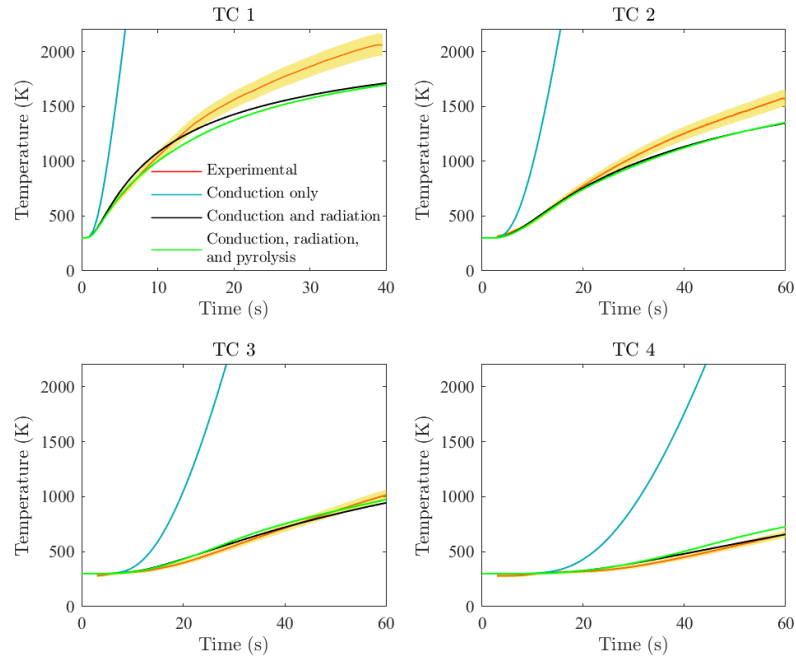


Figure 3.1: Axial TCs for models of increasing complexity along with experimental data,  $\alpha = 2.0$ .

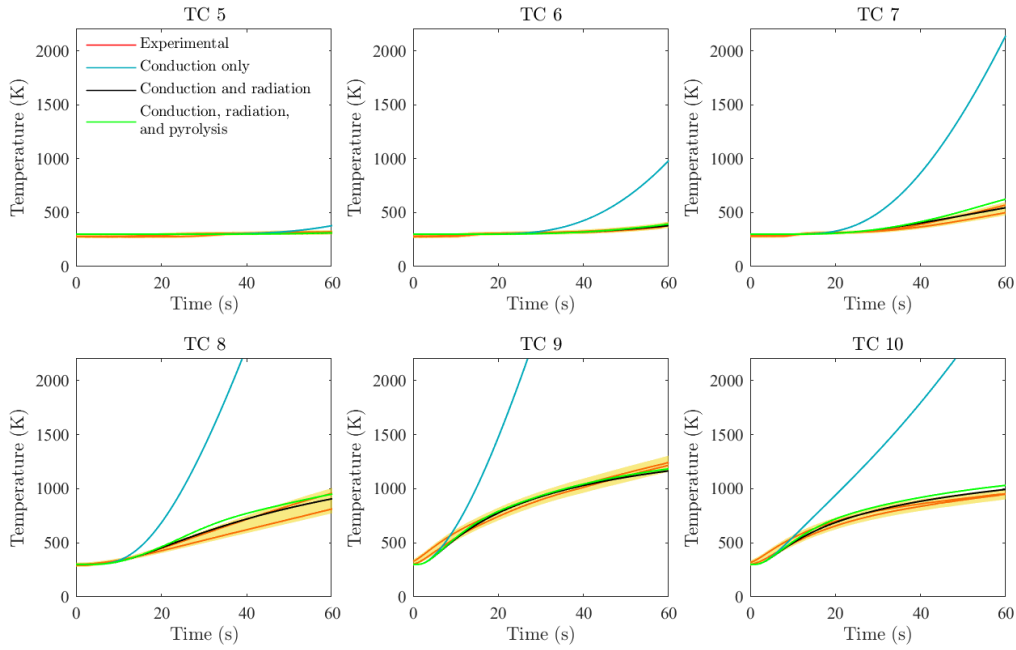


Figure 3.2: Radial TCs for models of increasing complexity along with experimental data,  $\alpha = 2.0$ .

Based on this, conduction alone was unable to provide a point of comparison even over short time spans near the surface. However, once radiation was implemented there was minimal difference between models which included pyrolysis and those which did not. Figs. 3.1 and 3.2 show results from a simulation which used the competitive material model, but using the FIAT1D model produces very similar results. A comparison of the thermal response using each model is shown in Figs. 3.3 and 3.4.

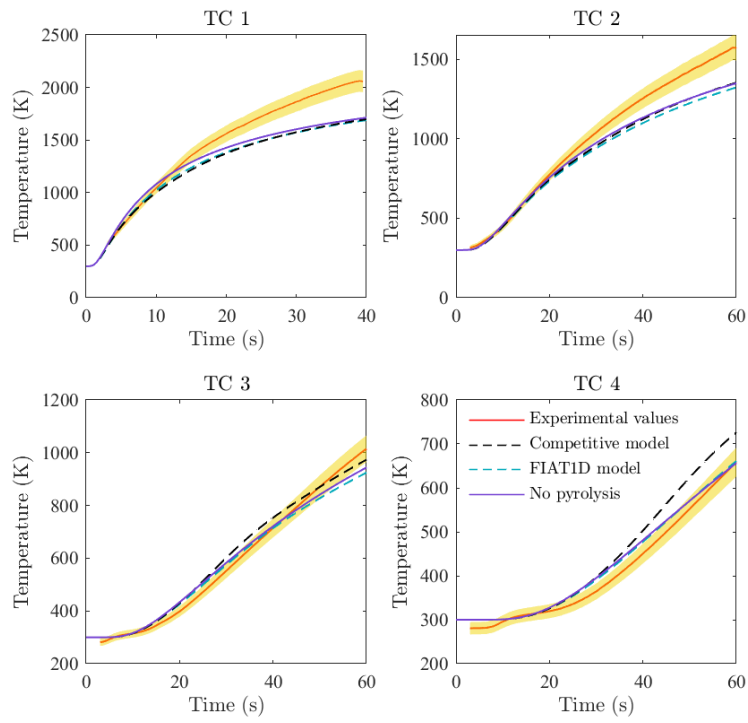


Figure 3.3: Axial TCs temperature response for different pyrolysis models.

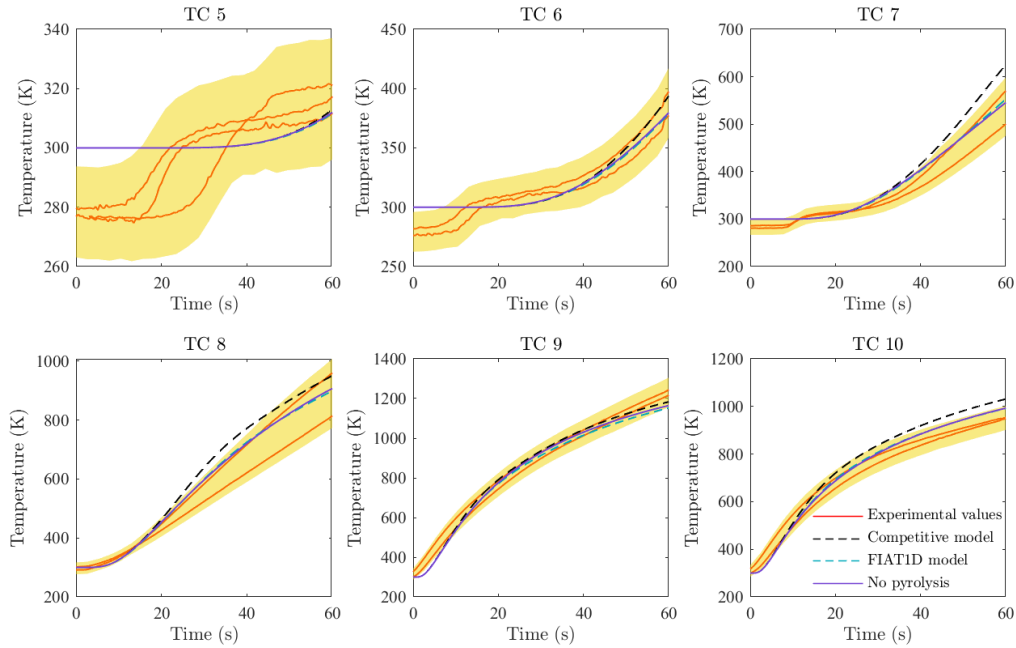


Figure 3.4: Radial TCs temperature response for different pyrolysis models.

These results indicate that at lower temperatures, the pyrolysis term acts as a source term rather than a sink (exothermic reactions). This is a consequence of the difference in specific enthalpy between solid and gas states at different temperatures through the pyrolysis source term in Eq. 2.1. Specific enthalpy values from Lachaud, et. al.'s Porous Material Analysis Toolbox based on OpenFOAM (PATO) [18–20] were used for values of char, virgin, and gaseous specific enthalpies for the Theoretical Ablative Composite for Open Testing (TACOT)[19, 21], a low density porous carbon and phenolic material which is similar to PICA but open-source. To clarify this point, specific enthalpies from the TACOT model are plotted below in Fig. 3.5.

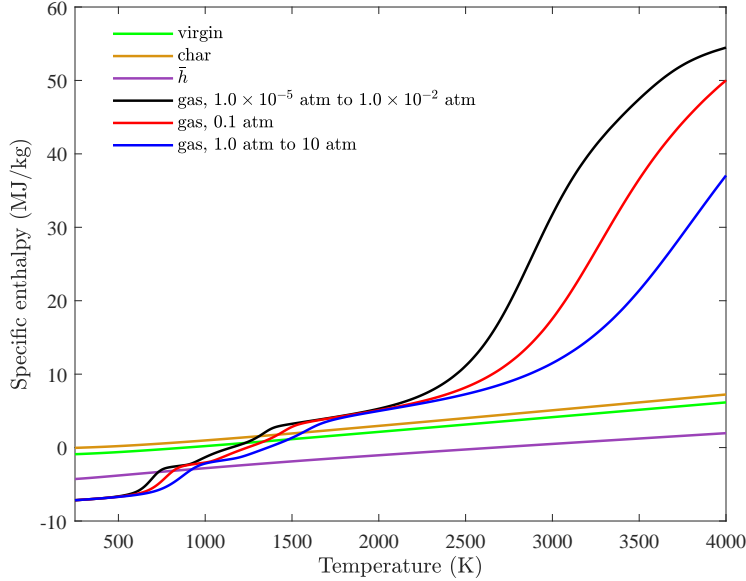


Figure 3.5: Specific enthalpy for TACOT.

The pyrolysis gas is modeled as a single gas with an enthalpy that depends on temperature and pressure. Previous experimental studies have confirmed that the specific enthalpy of char and virgin PICA are only weak functions of pressure and depend mainly on temperature [10]. Since the enthalpy change associated with pyrolysis is  $(h_g - \bar{h})\partial\rho_s/\partial t$ , where a positive value of  $h_g - \bar{h}$  corresponds to an endothermic reaction, it is helpful to plot this quantity as shown in Fig.3.6. The dashed horizontal line identifies the temperature range above which pyrolysis is modeled as an endothermic reaction. For conditions corresponding to 0.1 atm, this occurs at around 800 K.

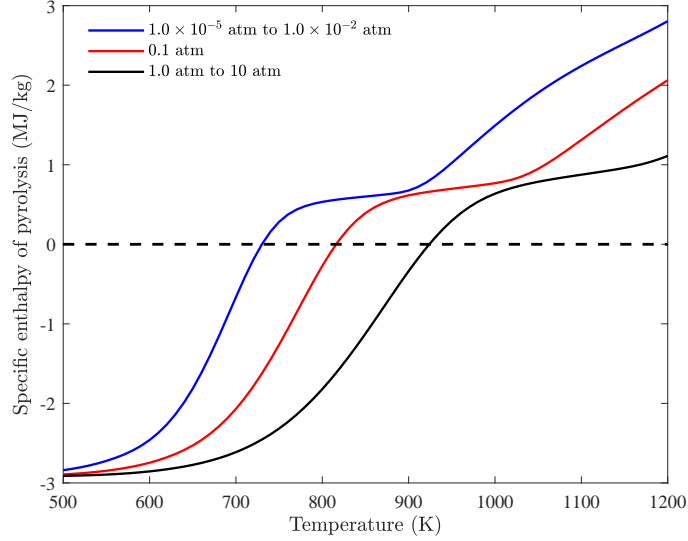


Figure 3.6: TACOT specific enthalpy of pyrolysis,  $h_g - \bar{h}$ .

To demonstrate heating rate effects on the competitive and the FIAT1D/CMA material models, consider the nominal average heating rate of approximately 30 K/s at TC1 and 3.7 K/s at TC5 corresponding to a linear increase from the initial temperature to the maximum experimental temperature. TC1 represents temperatures very close to the surface at the stagnation point, while TC5 represents temperatures deeper in the material along the centerline axis. Running a 0D simulation of the material response for the competitive model and the FIAT1D/CMA model at these conditions yields the rates of nondimensional density change shown in Fig. 3.7. For clarity, the opposite of nondimensional rate of change of density is plotted to yield positive values. The vertical line denotes the temperature at which reactions begin to be modeled as endothermic for a simulation test pressure of 0.1 atm.

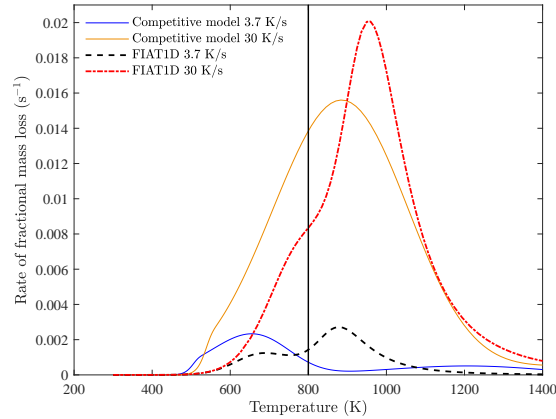


Figure 3.7: Rate of change of density for different material models,  $-\partial\tilde{\rho}_s/\partial t$ .

For the conditions that TC1 experiences, almost all density change due to pyrolysis is occurring at endothermic temperatures for both models. However, at TC5 the competitive model predicts that pyrolysis reactions will occur in an exothermic manner at a lower temperature. In contrast, FIAT1D/CMA results in most material loss occurring at endothermic temperatures at 3.7 K/s. Figure 3.7 also shows that both models predict that the maximum reaction rate will occur at higher temperatures when the heating rate is higher. The material models chosen were not intended to model all chemical kinetics rigorously but to provide an indication of the importance of pyrolysis, particularly early in the heating cycle. Specific reaction processes are still being researched; the initial small rise visible in the TC 5 experimental data, for example, has been theorized to result from an exothermic reaction not currently modeled [1]. Clearly, conductive and radiative effects dominate early on. To illustrate a potential reason for this, thermocouple data for the first few seconds of heating were compared to the solid density in the material at different times. By defining the extent of reaction as,

$$\tau = \frac{1 - \rho_c/\rho_s}{1 - \rho_c/\rho_v}, \quad (3.1)$$

and defining the pyrolysis zone as bounded by the contours where  $\tau = 0.02$  and  $\tau = 0.98$ ,

extent of pyrolysis is shown at 10 seconds and 20 seconds in Fig. 3.8

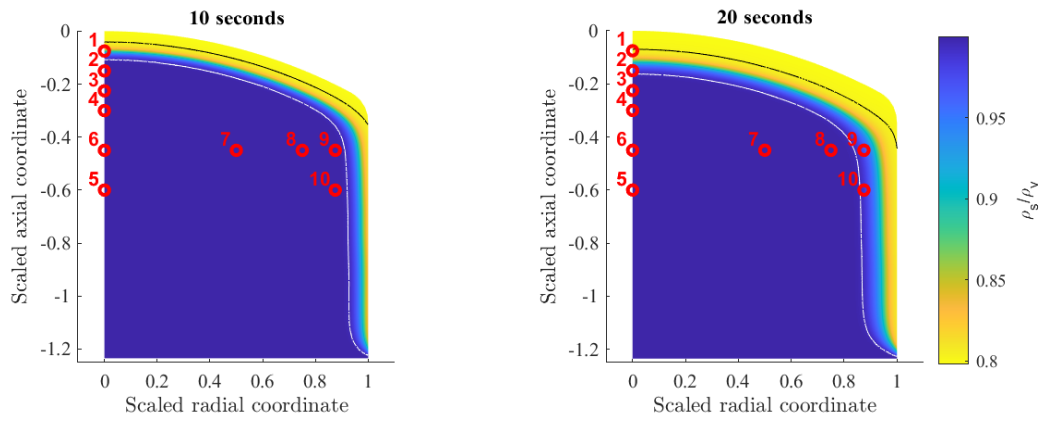


Figure 3.8: Solid density fraction remaining in the material, FIAT1D/CMA model,  $\alpha = 2.0$ .

From these plots, pyrolysis begins to affect TC 1 at around 10 seconds and begins to affect TCs 2, 9, and 10 at around 20 seconds. A comparison of the experimental data and simulation results for the first few seconds for select TCs is shown below in Fig. 3.9.

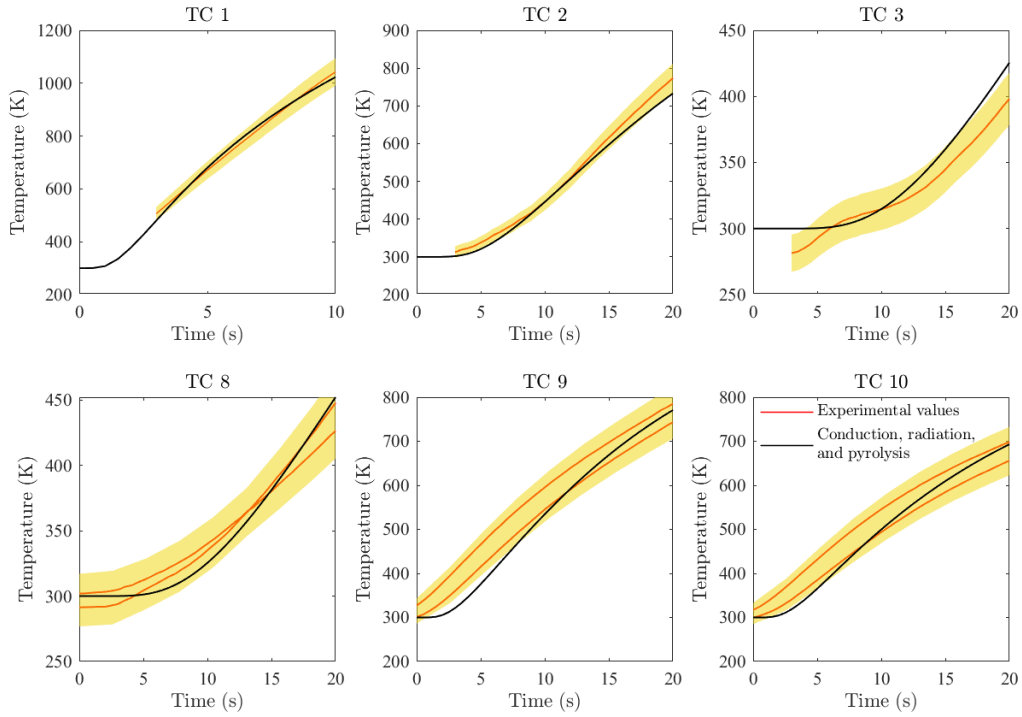


Figure 3.9: Temperature response close to the surface, FIAT1D/CMA model,  $\alpha = 2.0$ .

The initial temperature response of the thermocouples close to the surface at the stagnation point and along the side show general agreement with experimental data while outside of the pyrolysis zone or near its edge, and start to lose fidelity when pyrolysis becomes significant. Some differences between the simulation and experimental results are observed. Experimental thermocouple data in the axial direction are available after approximately two seconds, but there is evidently an initial inhomogeneous temperature distribution in the sample, with deeper thermocouples starting at lower temperatures. This may be due to radiative heating at the sample's surface prior to insertion into the arcjet. Furthermore, there may be a short translational period during which the arm holding the sample moves to the center of the arcjet[22]. This could result in sidewall heating affecting thermocouples nine and ten prior to the experiment start time, which is taken to be when the sample is at the arcjet center. While not necessarily significant

to the material response over longer periods, the uniform initial temperature assumption for the simulation seems to create marked differences from the initial experimental results. For accurate inference of material properties, the initial temperature distribution in simulations will need to match the initial temperature distribution in experiments.

### 3.2 Material property effects

To ascertain the effect of varying material properties, the simulation was also conducted with isotropic thermal conductivity ( $\alpha = 1.0$ ) using the competitive model for pyrolysis. These results are plotted in comparison to experimental data in Figs. 3.10 and 3.11.

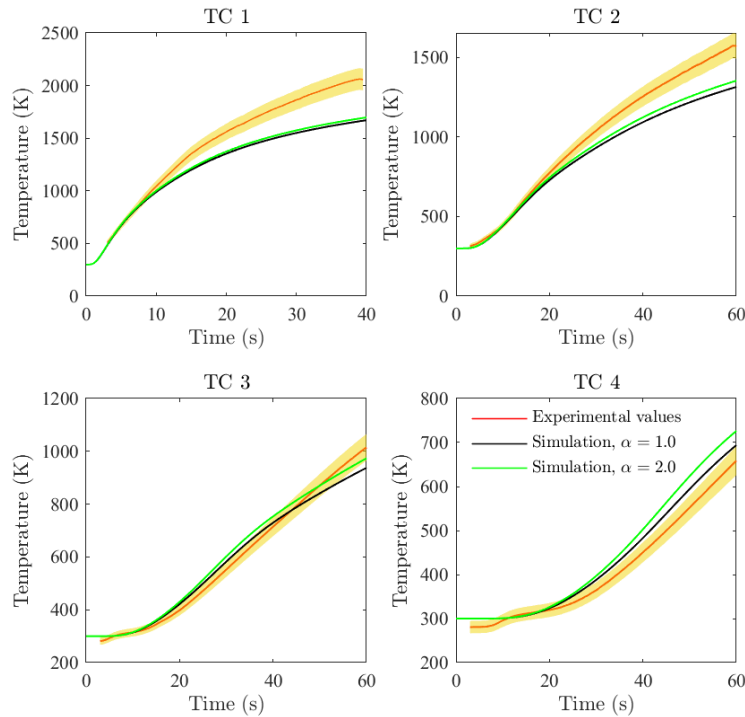


Figure 3.10: Axial TCs temperature response with conduction, pyrolysis, and radiation.

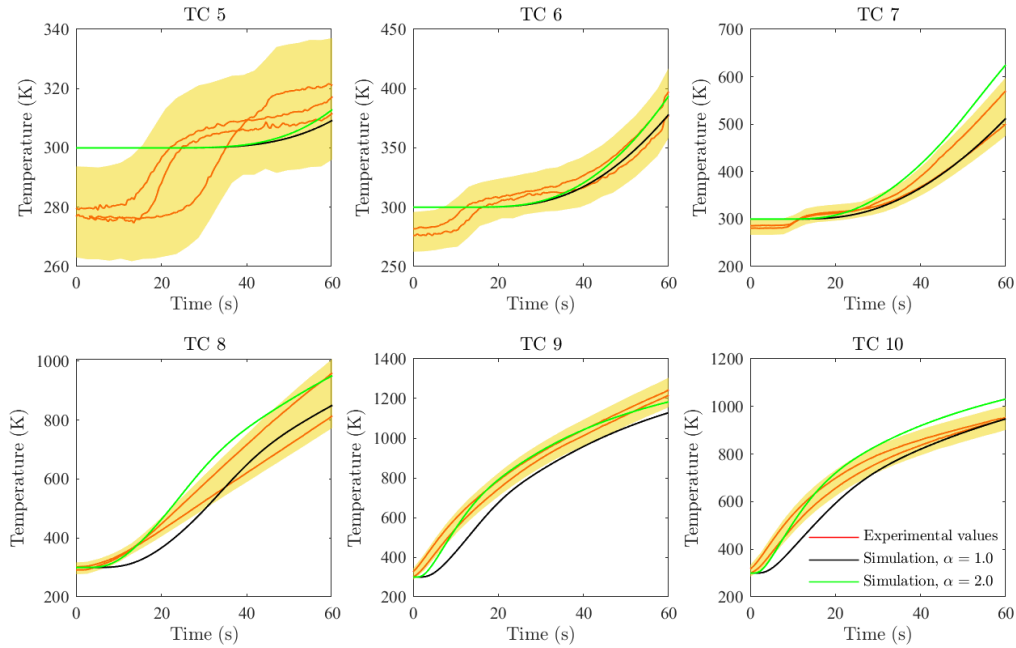


Figure 3.11: Radial TCs temperature response with conduction, pyrolysis, and radiation.

These figures show the expected result that changing the orthotropicity of the material results in minimal impact to the TCs along the model’s axis but changes the radial TC response substantially. For a higher in-plane thermal conductivity, the material experiences higher temperatures due to increased sidewall heating. This demonstrates the need for two-dimensional modeling for two-dimensional and axisymmetric heating profiles. It also shows that material response close to the sidewall is more sensitive to orthotropic effects than along the centerline axis. To investigate the effects of varying volumetric heat capacity, simulations were conducted with  $\rho C_p$  set to constant nominal values in virgin and char PICA. Specific heats are based on Covington, et. al.’s [14] PICA thermophysical properties for virgin material at low temperature and char material at high temperature as shown below in Table 3.1. These are also the values that PATO uses for its TACOT model. Densities for virgin and char material from PATO’s TACOT model were used.

Results for the thermocouple response in nondimensional values are shown below in Figs.

Table 3.1: Virgin and char material properties.

$\rho_v, \text{kg/m}^3$	$\rho_c, \text{kg/m}^3$	$C_{p,v}, \text{kJ/kg-K}$	$C_{p,c}, \text{kJ/kg-K}$
280	221	0.88	2.15

3.12 and 3.13 . These plots indicate that when considering dimensionless temperature and time, as long as  $\rho C_p$  is uniform throughout the material and constant in time, its only effect appears in the pyrolysis term and is relatively small. This behavior will not necessarily be the case when considering spatially and temporally non-uniform material properties, but it seems reasonable that the pyrolysis zone is small initially with spatial inhomogeneity in material properties minimal. The temperature response for these two cases in dimensional form, however, are substantially different as shown in Figs. 3.14 and 3.15, since  $\rho C_p$  is used in the definition of the reference time.

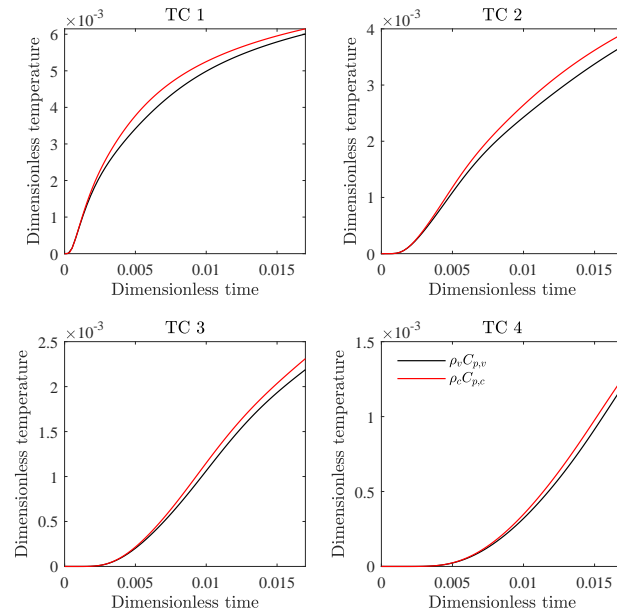


Figure 3.12: Axial TCs for differing material properties (dimensionless response).

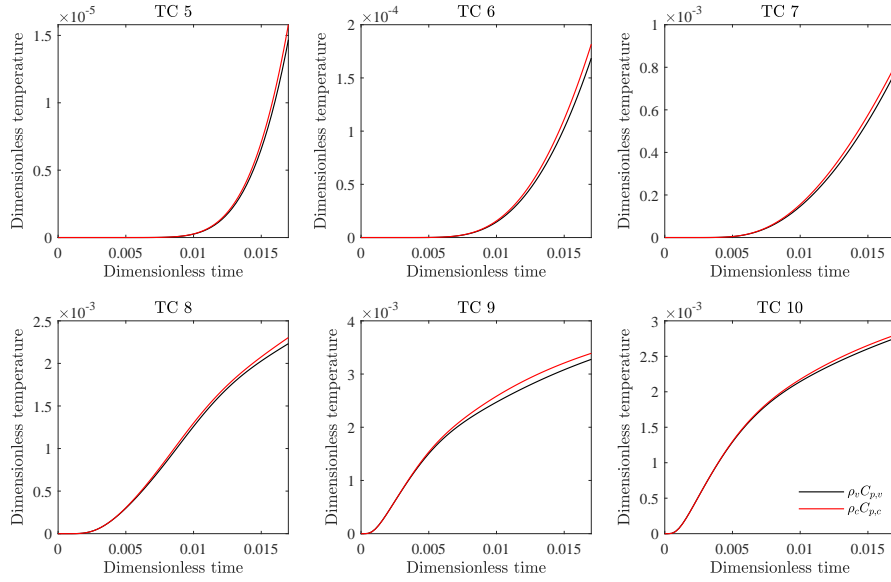


Figure 3.13: Radial TCs for differing material properties (dimensionless response).

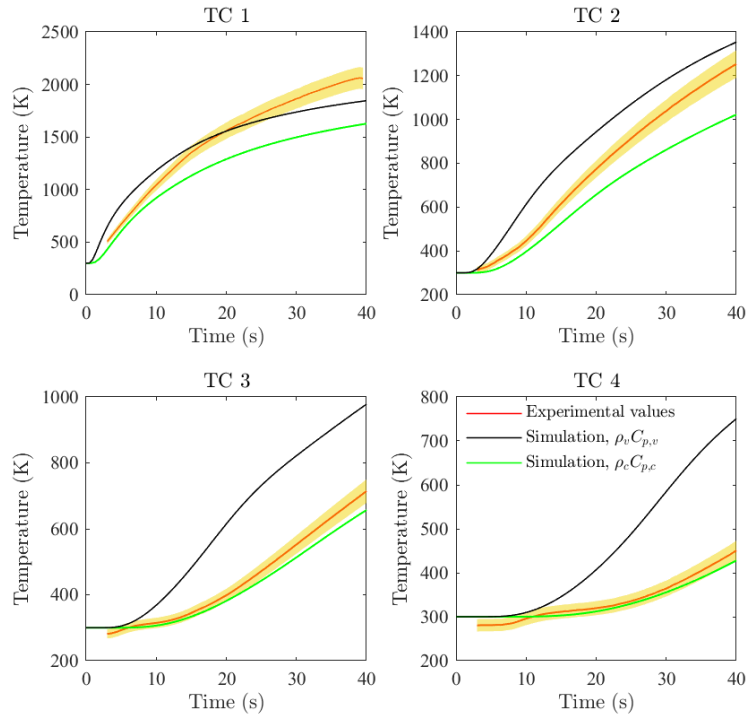


Figure 3.14: Axial TCs for differing material properties (dimensional response).

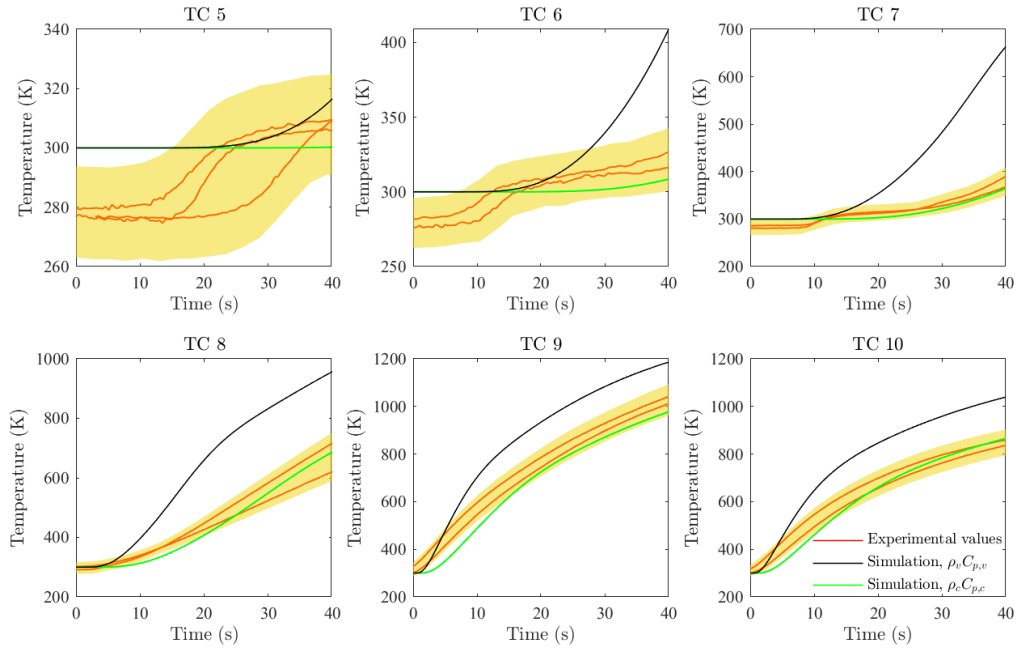


Figure 3.15: Radial TCs for differing material properties (dimensional response).

Figs. 3.10 through 3.15 help demonstrate how varying  $\alpha$  and  $\rho C_p$  changes the temperature response in the material, potentially allowing inference of these material properties through comparison to existing experimental data. For accurate inferences to be made, however, an accurate initial temperature distribution for the simulation appears to be needed.

As stated in section 2.1, our model neglects surface recession and ablative effects, pyrolysis gas flow, and nonuniform thermal conductivity and heat capacity effects, which leads to a divergence between simulation and experimental results when these are significant. In regards to the first of these, Milos and Chen found that a stagnation point cold-wall heat flux of  $169 \text{ W/cm}^2$  resulted in a stagnation point recession of over 4 mm over the course of 60 seconds, leading to the failure of TC1 [1]. The removal of surface material likely leads to higher temperatures throughout the material over time, but is especially noticeable in TC1.

The second of these, the effects of gas flow, can serve to convect cooler gases from the interior of the material to the surface and out of the material. The current approach assumes local thermal equilibrium between the gas temperature and the solid material, but previous simulations of reacting flows suggest this may not be a good assumption [5]. Also, the effects of pyrolysis gas mixing with the boundary layer can cause a reduction from the cold-wall heat flux value in heat transferred to a pyrolyzing material. This has most commonly been modeled in previous terms through use of  $B'$  tables which seek to model the reduction in heat transfer due to this phenomenon [6, 23].

Finally, both specific heat capacity and thermal conductivity vary based on temperature, which was not included here. Thermal conductivity is also a function of composition of the material; pure char is primarily carbon and has substantially higher thermal conductivity and specific heat capacity than virgin PICA [10, 14]. For this reason, this model will be most applicable for low heating rates with little temperature rise, as the effects of surface recession, pyrolysis gas convection, and changing material properties should be minimized in such a case. Within this regime, inference of  $\alpha$  and  $\rho C_p$  would be possible.

## Chapter 4

### Conclusion

Initial TPS material response to external heating can be modeled in a simplified manner with external heating, conduction, and radiation as the most important processes. Such a model can be used as part of an inference approach to material thermal conductivity and volumetric heat capacity in isolation. For best comparison, experiments with uniform initial conditions and very low heat loads applied are desired. Accurate inference will require accurate replication of the initial experimental temperature distribution if temperature inhomogeneities are found. Areas for further development include more exact replication of the initial conditions of existing experimental data and application of an inference scheme to calculate expected material properties for PICA.

## Bibliography

- [1] Milos, F. S., and Chen, Y.-K., “Ablation and Thermal Response Property Model Validation for Phenolic Impregnated Carbon Ablator,” *Journal of Spacecraft and Rockets*, Vol. 47, No. 5, 2010, pp. 786–805. <https://doi.org/10.2514/1.42949>.
- [2] Torres Herrador, F., Coheur, J., Panerai, F., Magin, T., Arnst, M., Mansour, N., and Blondeau, J., “Competitive kinetic model for the pyrolysis of the Phenolic Impregnated Carbon Ablator,” *Aerospace Science and Technology*, Vol. 100, 2020, p. 105784. <https://doi.org/10.1016/j.ast.2020.105784>.
- [3] Milos, F. S., and Chen, Y.-K., “Two-Dimensional Ablation, Thermal Response, and Sizing Program for Pyrolyzing Ablators,” *Journal of Spacecraft and Rockets*, Vol. 46, No. 6, 2009, pp. 1089–1099. <https://doi.org/10.2514/1.36575>.
- [4] Pavlosky, J. E., and St.leger, L. G., “Apollo experience report: Thermal protection subsystem,” Technical note tn-d-7564, NASA, Washington, D.C., 1974.
- [5] Scoggins, J. B., and Hassan, H. A., “Pyrolysis Mechanism of PICA,” *10th AIAA/ASME Joint Thermophysics and Heat Transfer Conference*, 2010. <https://doi.org/10.2514/6.2010-4655>.
- [6] Chen, Y.-K., and Milos, F. S., “Ablation and Thermal Response Program for Spacecraft Heatshield Analysis,” *Journal of Spacecraft and Rockets*, Vol. 36, No. 3, 1999, pp. 475–483. <https://doi.org/10.2514/2.3469>.
- [7] Beck, R. A. S., Driver, D. M., Wright, M. J., Hwang, H. H., Edquist, K. T., and Sepka, S. A., “Development of the Mars Science Laboratory Heatshield Thermal

- Protection System,” *Journal of spacecraft and rockets*, Vol. 51, No. 4, 2014, pp. 1139–1150.
- [8] Trick, K. A., and Saliba, T. E., “Mechanisms of the pyrolysis of phenolic resin in a carbon/phenolic composite,” *Carbon*, Vol. 33, No. 11, 1995, pp. 1509–1515. [https://doi.org/https://doi.org/10.1016/0008-6223\(95\)00092-R](https://doi.org/https://doi.org/10.1016/0008-6223(95)00092-R).
- [9] Tran, H., Johnson, C., Rasky, D., Hui, F., Hsu, M.-T., and Chen, Y., *Phenolic Impregnated Carbon Ablators (PICA) for Discovery class missions*, 1996. <https://doi.org/10.2514/6.1996-1911>.
- [10] Tran, H. K., Johnson, C. E., Rasky, D. J., Hui, F. Y. C., ta Hsu, M., Chen, T. S., Chen, Y.-K., Paragas, D., and Kobayashi, L., “Phenolic Impregnated Carbon Ablators (PICA) as Thermal Protection Systems for Discovery Missions,” Nasa technical memorandum 110440, 1997.
- [11] Clark, K. J., Flood, D. T., Moyer, C. B., and Rindal, R. A., “Experimental and Theoretical Analysis of Ablative Material Response in a Liquid- Propellant Rocket Engine Final Report,” Technical report, Aerotherm Corp., Palo Alto, California, 1967.
- [12] Agrawal, P., Ellerby, D. T., Switzer, M. R., and Squire, T. H., “Multidimensional Testing of Thermal Protection Materials in the Arcjet Test Facility,” *10th AIAA/ASME Joint Thermophysics and Heat Transfer Conference*, 2010. <https://doi.org/10.2514/6.2010-4664>.
- [13] Milos, F. S., and Chen, Y.-K., “Ablation and Thermal Property Model for Phenolic Impregnated Carbon Ablator (PICA),” Nasa tm 2009-215377, 3 2009.
- [14] Covington, M. A., Heinemann, J. M., Goldstein, H. E., Chen, Y.-K., Terrazas-Salinas, I., Balboni, J. A., Olejniczak, J., and Martinez, E. R., “Performance of

- a Low Density Ablative Heat Shield Material,” *Journal of Spacecraft and Rockets*, Vol. 45, No. 2, 2008, pp. 237–247. <https://doi.org/10.2514/1.12403>.
- [15] Moyer, C. B., and Wool, M. R., “Aerotherm Charring Material Thermal Response and Ablation Program, Version 3. Volume 1. Program Description and Sample Problems,” User’s manual, Aerotherm Corp., Mountain View, California, 1970.
- [16] Weng, H., and Martin, A., *Numerical Investigation of Pyrolysis Gas Blowing Pattern and Thermal Response using Orthotropic Charring Ablative Material*, 2014. <https://doi.org/10.2514/6.2014-2121>.
- [17] Squire, T. H., Milos, F. S. M., and Rasky, D. J., “TPSX: Thermal Protection System Expert and Material Property Database,” *ICCE Fourth International Conference on Composites Engineering*, ICCE and College of Engineering, University of New Orleans, 1997, pp. 937–938.
- [18] Lachaud, J., and Mansour, N. N., “Porous-Material Analysis Toolbox Based on OpenFOAM and Applications,” *Journal of Thermophysics and Heat Transfer*, Vol. 28, No. 2, 2014, pp. 191–202. <https://doi.org/10.2514/1.T4262>.
- [19] Lachaud, J., van Eekelen, T., Scoggins, J. B., Magin, T. E., and Mansour, N. N., “Detailed chemical equilibrium model for porous ablative materials,” *International Journal of Heat and Mass Transfer*, Vol. 90, 2015, pp. 1034–1045. <https://doi.org/https://doi.org/10.1016/j.ijheatmasstransfer.2015.05.106>.
- [20] Lachaud, J., Scoggins, J., Magin, T., Meyer, M., and Mansour, N., “A generic local thermal equilibrium model for porous reactive materials submitted to high temperatures,” *International Journal of Heat and Mass Transfer*, Vol. 108, 2017, pp. 1406–1417. <https://doi.org/https://doi.org/10.1016/j.ijheatmasstransfer.2016.11.067>.

- [21] Meurisse, J. B. E., Lachaud, J., Panerai, F., Tang, C., and Mansour, N. N., “Multi-dimensional material response simulations of a full-scale tiled ablative heatshield,” *Aerospace Science and Technology*, Vol. 76, 2018, pp. 497–511. <https://doi.org/https://doi.org/10.1016/j.ast.2018.01.013>.
- [22] Terrazas-Salinas, I., “Test Planning Guide for NASA Ames Research Center Arc Jet Complex and Range Complex,” Planning Guide A029-9701-XM3 Rev. C, NASA Ames Research Center, Moffett Field, CA 94035, April 2009.
- [23] Milos, F., and Chen, Y.-K., “Comprehensive model for multicomponent ablation thermochemistry,” *35th Aerospace Sciences Meeting and Exhibit*, AIAA 1997-141, 1997. <https://doi.org/10.2514/6.1997-141>.